OPEN ACCESS
IOP Publishing
Journal of Physics: Condensed Matter
J. Phys.: Condens. Matter **37** (2025) 465001 (12pp)
https://doi.org/10.1088/1361-648X/ae14c8

Enhanced chemical vapor deposition of monolayer MoS_2 films via a clean promoter

Lulin Wang[1,2,*], Yue Sun[1,2], Kaushik Kannan[1,2], Lee Gannon[1,2], Xuyun Guo[2,3], Aran Rafferty[2,3], Karl Gaff[1], Navaj B Mullani[1,2], Haizhong Weng[1,2], Yangbo Zhou[4], Valeria Nicolosi[2,3], Cormac McGuinness[1,2], Peter Gleeson[5] and Hongzhou Zhang[1,2,*]

[1] School of Physics, Trinity College Dublin, Dublin 2, Ireland
[2] CRANN and AMBER Research Centers, Trinity College Dublin, Dublin 2, Ireland
[3] School of Chemistry, Trinity College Dublin, Dublin 2, Ireland
[4] School of Physics and Materials Science, Nanchang University, Nanchang 330031, People's Republic of China
[5] Intel Foundry Technology Research Ireland, Leixlip, Co., Kildare, Ireland

E-mail: wangl9@tcd.ie and hozhang@tcd.ie

Received 13 August 2025, revised 16 September 2025
Accepted for publication 17 October 2025
Published 11 November 2025

Abstract

Two-dimensional (2D) transition metal dichalcogenides, exemplified by molybdenum disulfide (MoS_2), have shown exceptional potential for data-centered, energy-efficient electronic applications due to their unique electrical, optoelectronic, and mechanical properties. However, challenges such as the controllable synthesis of high-quality, large-area 2D MoS_2 films and the mitigation of contamination during growth remain significant barriers to their integration into advanced technologies. Here, photoresist S1813 is innovatively utilized as a contamination-free growth promoter, enabling the clean and scalable synthesis of high quality 2D MoS_2 on SiO_2/Si substrate with desirable grain structures via chemical vapor deposition. By optimizing the reactant concentration and S/Mo ratio, enhanced MoS_2 growth with improved quality is achieved, as evidenced by the increased MoS_2 flake size and coverage, alongside a strong photoluminescence A exciton peak at 1.84 eV. This approach facilitates the clean and selective growth of high-quality 2D MoS_2, establishing a robust pathway for the practical implementation of 2D MoS_2 in next-generation electronic devices.

Supplementary material for this article is available online

Keywords: 2D materials, transition metal dichalcogenides, molybdenum disulfide, chemical vapor deposition

* Authors to whom any correspondence should be addressed.

1. Introduction

Two-dimensional (2D) transition metal dichalcogenides (TMDs) have emerged as promising candidates for next-generation electronic and optoelectronic devices, with emphasis on scaling and low-energy consumption applications, including logic transistors [1–5], photodetectors and lasers [6–8], and advanced neuromorphic devices [9, 10]. To ensure compatibility with industrial applications, it is crucial to achieve precise device control and minimize variability, which demands a controllable and scalable synthesis method for monolayer MoS_2.

Chemical vapor deposition (CVD) is recognized as one of the most promising approaches for scalable synthesis of MoS_2 [11]. The epitaxial growth of MoS_2 on sapphire substrates has garnered considerable attention for achieving wafer-scale MoS_2 films [12–15]. However, the as-synthesized MoS_2 requires an additional transfer step to relocate onto other arbitrary target substrates for further device fabrication, which may inevitably introduce contamination and strain that potentially alter or deteriorate the intrinsic properties of the film. Recently, the 2D Czochralski method [16] achieved uniform single-crystal MoS_2 with centimeter-scale domains on a molten glass substrate. While the etching-free transfer process is cleaner than the conventional wet transfer, it may still introduce strain, and the substrate introduced contamination (e.g. Na^+) remains unverified. Synthesizing MoS_2 directly on SiO_2/Si substrates provides a solution to these transfer and substrate related issues. However, the absence of epitaxial templating of MoS_2 on the amorphous SiO_2 surface makes it challenging to control the nucleation and large-scale synthesis of single-crystal MoS_2, resulting in random nucleation and other inhomogeneities [4]. Therefore, a clean approach for controlling MoS_2 nucleation and enhancing lateral film growth on amorphous SiO_2 substrate needs to be developed.

To facilitate the 2D growth of MoS_2, seeding promoters are introduced to the substrate prior to the CVD process. For instance, alkali metal halides (e.g. NaCl [17], KI [18]) and hydrates (e.g. NaOH [19]) have been reported to reduce the reaction temperature and weaken the interlayer adhesion, thereby enhancing the lateral growth of MoS_2 film. Similarly, wafer-scale 2D MoS_2 films are achieved when alkaline-earth metal chlorides (e.g. $CaCl_2$, $SrCl_2$ [20]) are introduced in the CVD process. However, the residual metal ions from those promoters are detrimental to the electric properties of the MoS_2 film and it is found that compared to alkali-free synthesis under the same growth conditions, the utilization of NaCl can lead to variation in growth rates, loss of epitaxy, and dense clusters of nanoscale MoS_2 particles [21]. In addition, the alkali metal compounds lack the ability to control nucleation sites.

Alternatively, organic promoters such as perylene-3,4,9,10-tetracarboxylic acid tetrapotassium salt (PTAS) lead to millimeter size growth of 2D MoS_2, owing to the enhanced substrate adhesion of MoS_2 and heterogeneous nucleation sites [22–24]. However, uniformly applying PTAS on hydrophobic substrates poses challenges [24]. A thin film of polymer complex comprised of anhydrous ammonium tetrathiomolybdate and linearpoly (ethylenimine) has been found to effectively improve the growth uniformity and control the thickness of MoS_2 film in the range of 2–30 nm [25]. Nevertheless, precise control of the MoS_2 film thickness down to monolayer dimensions is still challenging. On the other hand, $F_{16}CuPc$ has been shown to significantly enhance MoS_2 growth compared to other organic promoters due to its thermostability [24]. It is worth mentioning that non-volatile species, such as potassium in PTAS and copper in $F_{16}CuPc$, may be retained in the MoS_2 film, thus altering its intrinsic properties. Furthermore, the cleanliness of the film growth in previous reports is not thoroughly understood, and the absence of promoter-induced contamination is not yet well demonstrated.

Here, we developed a contamination-free method to realize the controlled growth of large-scale monolayer MoS_2 on an amorphous SiO_2 substrate. The growth, facilitated by nano promoters, yields MoS_2 free of contamination as confirmed by x-ray photoelectron spectroscopy (XPS) and Raman spectroscopy. The effect of the promoter is evaluated by modifying half of the substrate with nano promoters, whilst keeping all other growth parameters the same. A notable promoter effect is observed at a sulfur temperature of 250 °C, where the promoter modified region preferentially facilitates the growth of individual single-crystal monolayer MoS_2 flakes with over 3 times the total coverage and a sixfold increase in the monolayer ratio. The proportion of large flakes ($\geqslant 10\ \mu$m) found in the promoter region is 60 times that of the pristine region. Furthermore, we systematically investigated the promoter effect at varied reactant concentrations by tuning the sulfur temperature, demonstrating the transition from homogeneous nucleation to heterogeneous nucleation. In addition, we also found that the sulfur temperature greatly affects the sulfur vacancy density in MoS_2. Our results offer a novel strategy to achieve clean and controllable growth of large-scale 2D MoS_2 on amorphous SiO_2 substrates, establishing a solid groundwork for advancing the controllability and the performance of 2D electronic devices.

2. Results and discussion

2.1. The promoter effect: enhanced 2D growth

The growth is achieved via the CVD method with the assistance of polymer nano promoters. Specifically, the promoter is a conventional photoresist S1813 (Shipley), which consists of cresol novolak resin and a photoactive compound [26]. To investigate the promoter effects, the substrate surface is divided into two regions: one decorated by the promoter, the other kept pristine (figure S1). In a typical growth process (see figure 1(a) top panel), 1 mg of MoO_3 powder (Afla Aesar, 99.9%) is placed in a quartz crucible with an angled groove ($\theta = 120°$) relative to the tube axis. The substrate is placed within the groove, 0.5 cm downstream from the MoO_3 powder. Additionally, 120 mg of sulfur powder is placed in a separate crucible (see figure S2). Both crucibles are loaded into

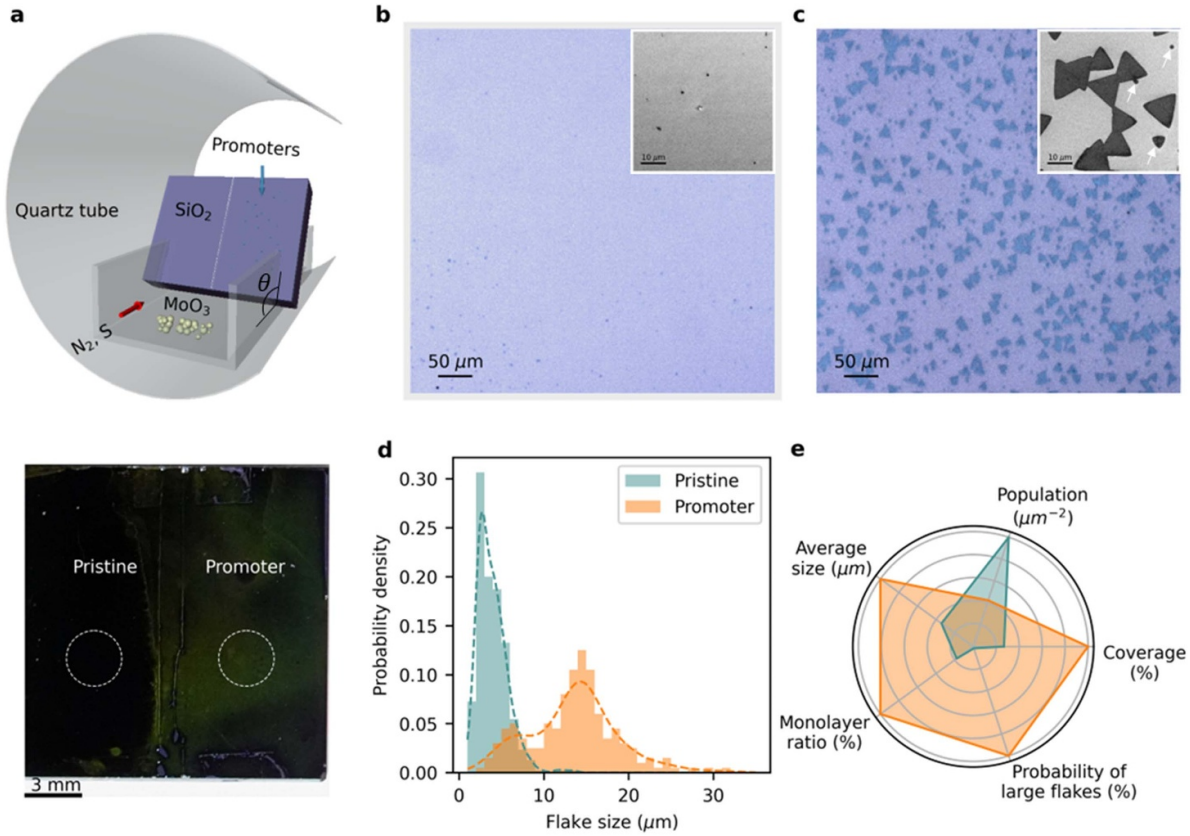

Figure 1. A typical promoter-assisted CVD growth of MoS_2 at a sulfur temperature of 250 °C. (a) Top panel: an illustration of the key growth configuration. $\theta = 120^\circ$ is the angle between the substrate and the upstream direction relative to the tube axis. Bottom panel: An optical image of the wafer coupon post-growth. The white dashed circles highlight two equivalent regions—one from the pristine region and the other from the promoter region—under similar growth conditions, such as reactant concentration and flow. Optical micrographs with SEM images provided in the insets: (b) the pristine substrate which remain clean and (c) the promoter region covered by triangular MoS_2 flakes. The white arrows in the inset of (c) indicate small flakes. (d) Statistical distribution of flake sizes comparing the growth in the pristine and promoter regions. (e) A radar chart comparing the average flake size, monolayer ratio, probability of large flakes, coverage and population density for the pristine substrate and promoter regions.

the furnace with each crucible's temperature controlled independently. The heating controller of sulfur is then energized when the substrate temperature reaches 765 °C. During the growth process, the substrate/MoO_3 temperature is maintained at 835 °C, and the sulfur temperature is kept at 250 °C for 5 min. Nitrogen gas is introduced as a protective and carrier gas at a flow rate of 20 sccm throughout the reaction period. Detailed information on substrate preparation and the CVD process can be found in the methods section.

We observe that the distance between the molybdenum source and the deposition site on the substrate can affect the growth behavior due to variations in gaseous reactant concentration and flow. As such, for a set of growth parameters, we compare the growth behaviors at two equivalent locations sampled from the pristine and promoter regions of the substrate, which are subject to an equivalent reaction environment. The most significant growth enhancement is observed by comparing two such equivalent regions near the bottom of the substrate and close to the crucible side walls. These regions, indicated by the dashed circles in the bottom panel of figure 1(a), are located 12 mm from the molybdenum source. The promoter region (right) exhibits a distinctly different color compared with the pristine region (left). A continuous dark olive-green film is visible on the surface of the promoter region, while the contrast of the pristine surface is close to that of the bare SiO_2/Si substrate. The difference in optical contrast suggests that, at the macroscopic scale, the promoter region has significantly more growth than the pristine region.

The optical micrographs of the pristine region (figure 1(b)) and promoter region (figure 1(c)) corroborate the observations made through visual inspection. Sparse micrometer-sized particles are present in the pristine region with diminished 2D growth. In contrast, the promoter region features a uniform distribution of triangular MoS_2 flakes. Some triangular flakes merge and form films up to approximately 33 μm in size. Optical micrographs with a field of view of 500 μm × 500 μm were further used for statistical analysis, which is conducted using Python [27]. Considering the resolution of the optical microscope, flakes larger than 2 μm are counted. Approximately 534 small particles are identified in the pristine region, compared with about 224 μm-sized flakes in the promoter region (figures S4(a) and (b)). The histogram

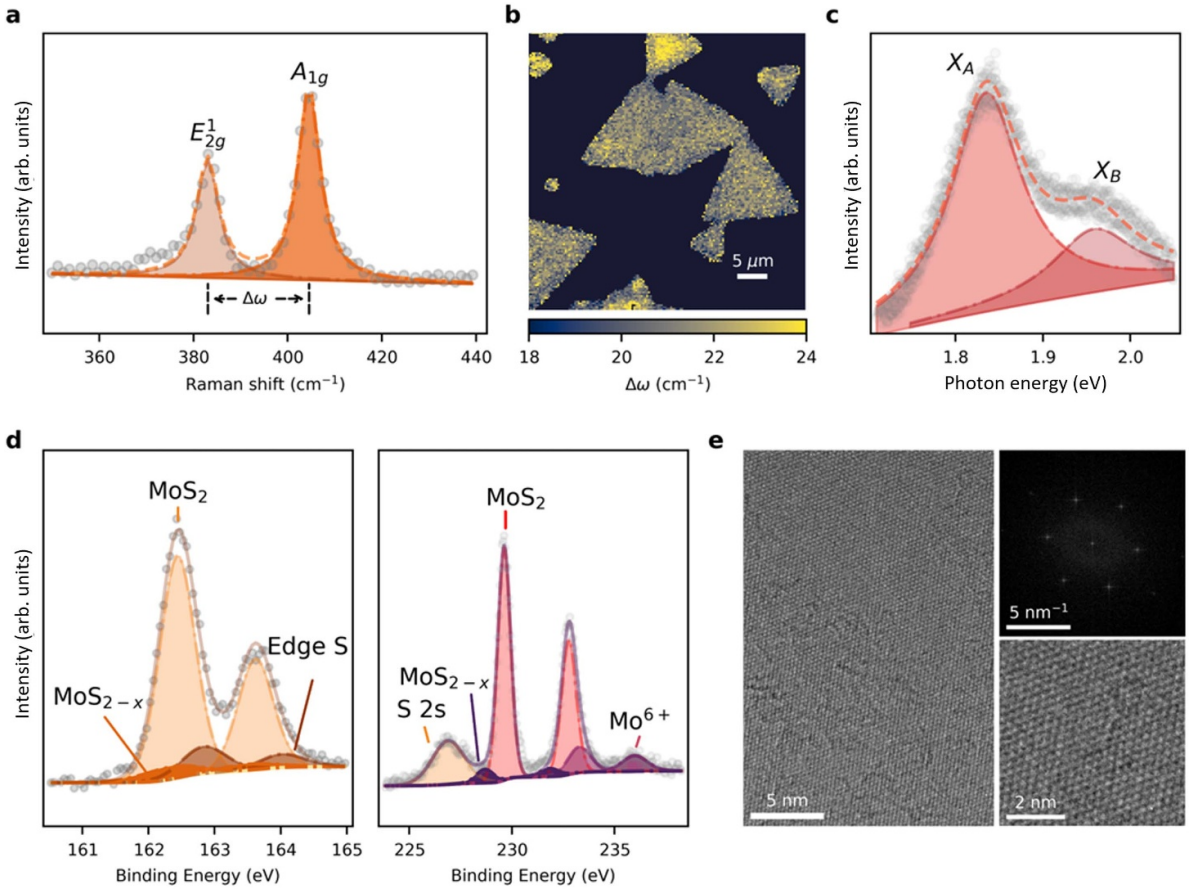

Figure 2. Characterizations of the MoS_2 flakes in the promoter region under sulfur temperature of 250 °C. (a) The average Raman spectrum shows E^1_{2g} and A_{1g} modes of 2H MoS_2 at 384.3 cm^{-1} and 405.1 cm^{-1} with a peak spacing of 20.8 cm^{-1}. (b) The mapping of the peak position difference shows the high population of monolayer flakes. (c) Averaged PL spectrum shows strong A exciton at 1.845 eV indicating the direct band gap MoS_2 which corresponds to the behavior of monolayer MoS_2. (d) XPS core-level spectra of Mo 3*d* and S 2*p*, where the main peaks show the chemical bond in 2H MoS_2. (e) HRTEM shows the lattice planes of MoS_2. The top right panel is the Fourier transform of the HRTEM image, which implies a single crystalline hexagonal structure. The zoom-in HRTEM image in the bottom right panel confirms the disorder-free lattice and the 2H phase.

in figure 1(d) illustrates that the flake size distribution in the pristine region follows a lognormal pattern with an average size of 3.9 μm (flake recognition see figure S4(a)). The promoter area exhibits a bimodal Gaussian distribution, where the first peak at 6.4 μm corresponds to the small flakes (as marked by white arrows in figure 1(c) and shown in figure S4(c)), which overlaps with the peak of the pristine region, indicating homogenous nucleation. The main peak at 14.4 μm represents the large triangular flakes (figure S4(d)), which is more than 3 times larger than the pristine region, indicating the heterogeneous nucleation induced by the nano promoters. Figure 1(e) compares five key characteristics of CVD growth, including the average size. The monolayer ratio, defined as the area ratio of monolayer MoS_2 to the total recognized area (figures S4(a) and (b)), of the promoter region is 88.9%, approximately six times higher than that of the pristine region. The abundance percentage of large flakes (>10 μm) is 30.2% in the promoter region and 0.5% in the pristine region. The coverage, defined as the ratio of the area covered by flakes to the total substrate area in the image, is significantly higher in the promoter region at 15.0%, almost four times that of the pristine region (4.0%). However, the population density, representing the number of flakes or particles per unit area, is lower in the promoter region (1.0×10^3 mm^{-2}) than in the pristine region (2.4×10^3 mm^{-2}). These quantitative statistical results confirm the enhanced growth of 2D MoS_2 in the promoter region.

The MoS_2 flakes in the promoter region are further characterized by Raman spectroscopy and photoluminescence (PL). As shown in figure 2(a), the average Raman spectrum exhibits two significant peaks at 384.3 cm^{-1} and 405.1 cm^{-1} which correspond to the E^1_{2g} and A_{1g} modes of 2H MoS_2, respectively. The spacing, $\Delta\omega$, between the two Raman modes is 20.8 cm^{-1} whereas the peak intensity ratio of E^1_{2g} and A_{1g} is 0.72. These results again indicate the monolayer nature of the MoS_2 flake [28–31]. Additionally, from the full-range Raman spectrum (figure S6(a)), no peak is observed in the Raman spectrum range of 1100–2000 cm^{-1}, indicating the absence of carbon residue [32]. A weak longitudinal acoustic (LA) peak

can be observed in the range of 210–250 cm^{-1}, characteristic of defect-induced Raman modes [33]. A map of the $\Delta\omega$ is shown in figure 2(b). The majority (∼95%) of the flakes in the mapping region exhibit consistent values of $\Delta\omega \sim 20$ cm^{-1}, suggesting a high population density of monolayer flakes. However, around 5% of areas show $\Delta\omega \sim 22$ cm^{-1}, which is attributed to bi-layer MoS_2. The monolayer ratio is consistent with the optical contrast result in figure S6(b). Additionally, secondary nucleation is evident in the scanning electron microscopy (SEM) image shown in figure S6(c). In the PL spectrum (figure 2(c)), a strong luminescence band appears at 1.845 eV and corresponds to the direct excitonic transition energy (A exciton) [2], indicating the direct band gap of the monolayer MoS_2 [3]. Moreover, a weak B exciton resonance is observed at 1.97 [3]. The Xa position mapping and intensity mapping (figure S7) show a uniform distribution across most of the flakes, which indicate minimal residuals or doping. A slight blue shift of Xa peak is observed at the flake edges, which is attributed to edge effect [34]. PL intensity enhanced at the boundaries between adjacent flakes is likely due to the presence of grain boundaries (GBs) [35]. Neither feature correlates with nucleation sites. The thickness of the flake is further verified through atomic force microscopy (AFM) measurement as shown in figure S6(d). The line profile in figure S6(e) indicates that the MoS_2 film thickness is 0.68 nm.

Figure 2(d) shows the XPS of core level spectra S 2*p* and Mo 3*d* spectra of the films in the promoter region. In the S 2*p* core-level spectrum, the doublets at 162.4 eV and 163.6 eV indicate the chemical states of S in 2H MoS_2 [4, 36]. The weak peaks at 164.1 eV and 162.9 eV can be attributed to the edge sulfur [37]. The doublet at 162.3 eV and 163.5 eV corresponds to the reduced chemical state of S, indicating a $MoS_{2\text{-}x}$ phase. In the Mo 3*d* core level spectrum, the doublets at 229.6 eV and 232.8 eV correspond to the chemical states of Mo in 2H MoS_2 [4, 36, 38]. The relative weak peaks at 233.3 eV and 236.0 eV correspond to the Mo^{6+}, implying the presence of a small amount of MoO_3. Doublet at 228.70 eV and 231.84 eV corresponds to the MoS_{2-x} phase. The peak at 227.0 eV is attributed to the S 2*s*. The results suggest that the film primarily consists of 2H MoS_2, with detectable sulfur vacancies and oxides species. For completeness, we investigate the particles grown in the pristine region. As shown in figures S8(a)and (b), the XPS spectra of the pristine region show a weak signal in the range of 224–239 eV (Mo 3*d* core level), while no peak is detected within the binding energy range of 162–164 eV (S 2*p* core level). This suggests the presence of a small amount of molybdenum compound but no detectable MoS_2. Moreover, figures S8(c) and (d) show the morphology of the pristine particles and the corresponding Raman spectrum. The characteristic peaks at 203, 233, 363, 464, 496, 570, and 744 cm^{-1} in figure S8(d) suggest that the particles are crystallized in the MoO_2 phase [39, 40]. We note that molybdenum oxide can, in principle, undergo sulfurization in the absence of growth promoters. However, the formation of MoO_2 rather than MoS_2 suggests an incomplete sulfurization reaction, with no detectable MoS_2 in the pristine region. The high-resolution transmission electron microscopy (HRTEM) image in figure 2(e) reveals the lattice structure of 2H MoS_2, taken from the area highlighted in low magnification images, figures S9(a) and (b). The six-fold symmetry is evident in the Fourier transform of the image shown in the top right panel of figure 2(e). The 2D lattice shown in the bottom right panel confirms the high-quality lattice structure and corroborates the 2H phase. The optical properties, chemical state and the lattice structure confirm that the flakes are monolayer 2H MoS_2.

To verify the cleanliness of the promoter-enhanced CVD method, XPS C 1*s* and O 1*s* core-level spectra are analyzed and compared in figure S10. For both the pristine and promoter regions, in the O 1*s* core-level spectra shown in figures S10(a) and (b), the main peak at 533.2 eV represents the O–Si bond which arises from the substrate. The weak peaks at 532.2 eV and 531.0 eV correspond to O–C and O–Mo bonds [41]. In the C 1*s* core-level spectra (figures S10(c) and (d)), a prominent peak appears at approximately 285.0 eV for both the pristine and promoter regions, corresponding to C–C bonds. In addition, peaks at around 286.5 eV, 288.0 eV and 289.2 eV correspond to the C–O single bonds, C=O double bonds and O–C=O bonds, respectively. These peaks are typical for adventitious carbon [42, 43] which is usually found on the surface of most air-exposed samples. There is no evidence to show that C and O bond with Mo or S (for example, C–Mo bonds in C 1 *s* at 284.2 eV [43, 44], C–S–C in S 2*p* at 163.5 eV and 164.8 eV [45]). The adventitious C signal is stronger in the promoter region than in the pristine region. A comparison of C 1*s* core-level spectra of the bare SiO_2 substrate and the bulk MoS_2 (figures S10(e) and (f)) shows consistently higher C intensity on MoS_2. This implies stronger C adsorption on the MoS_2 surface than the SiO_2 possibly due to the lower surface energy of MoS_2 relative to SiO_2 [46, 47]. The results confirm the cleanliness of the nano promoter-assisted growth.

2.2. *Effects of the sulfur-source temperature*

To further investigate the effect of the promoter, we examined the evolution of the morphology and yield of MoS_2 as a function of the sulfur temperature. The morphology of the CVD products (figure 3(a)) in the promoter region varies depending on the sulfur temperature. When the temperature is 180 °C, hexagonal MoS_2 flakes with rounded edges and a size of approximately 3 μm are observed, indicating insufficient sulfur concentration. As Ts increases to 200 °C, the MoS_2 flakes transition to a triangular shape with soft edges, suggesting an increase in sulfur concentration though it remains inadequate [48, 49]. At 220 °C, the triangular flakes grow larger and exhibit straighter edges. Further increasing to 250 °C results in uniformly distributed triangular MoS_2 flakes with increased flake size and well-defined straight edges. This indicates that the reactant concentration is sufficient for the 2D growth of stoichiometric MoS_2. For a temperature of 270 °C, the flakes show irregular shapes with sizes ranging from 0 to 30 μm, indicating the merging of multiple grains. The darker contrast at their center suggests excessive growth of multilayer

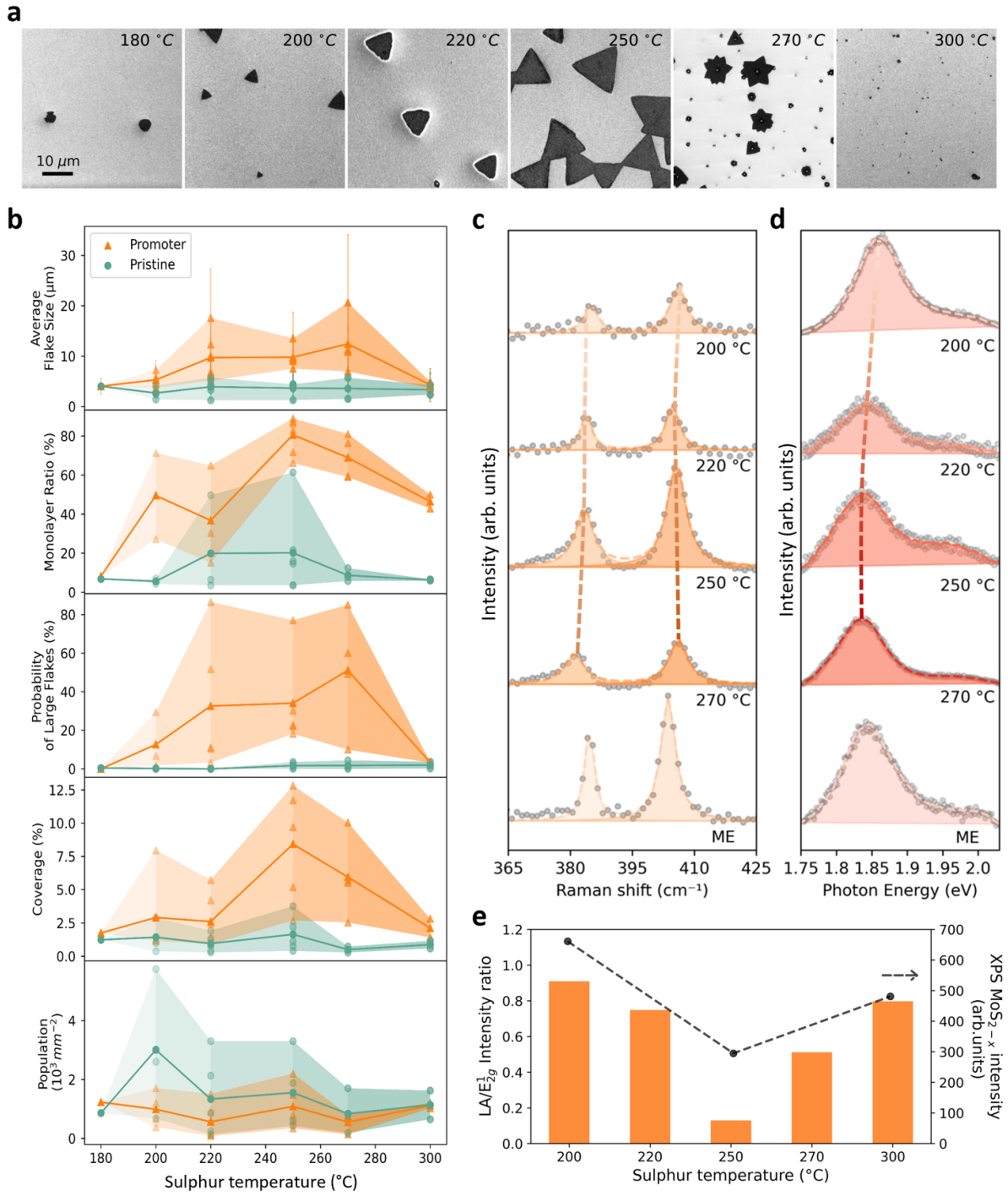

Figure 3. MoS_2 properties at varied sulfur temperature. (a) SEM images of samples in the promoter region. The SEM image of 250 °C is taken from the same region as insert of figure 1(c). (b) Statistic results of MoS_2 average flake size, monolayer ratio, probability of large flakes, coverage and population density, which are based on large-area optical images shown in figure S11. The orange triangle represents the promoter side, while the green circle corresponds to the pristine side. Each data point represents a measurement from an independently reproduced sample, and the solid line represents the average value. For a given temperature, sample number n = 4-6. The error bars in the top panel represent the standard deviation of multiple fakes from each sample. (c) Average Raman spectra of CVD MoS_2 and ME monolayer MoS_2. The spectra are normalized against the Si peak at 520 cm^{-1} and fitted by Lorentzian function. (d) Average PL spectra of CVD MoS_2 and ME monolayer MoS_2. (e) Defect analysis of samples prepared at 200 °C to 300 °C by Raman LA/E^1_{2g} peak intensity and XPS MoS_{2-x} phase intensity.

films, accompanied by the appearance of particles. Finally, at 300 °C, the MoS_2 appears as particles and submicron-sized triangular flakes. The presence of particles rather than the formation of films suggests that the nucleation rate has exceeded the growth rate.

Further statistical analysis, derived from the optical images in figure S11 and summarized in figure 3(b), compares five key growth metrics in the pristine and promoter regions. Multiple data points at a given temperature represent distinct samples grown under identical parameters, with error bars indicating the variation among flakes within each sample. The average flake size in the pristine region remains consistently within the range of 3-5 μm across all temperatures. In the promoter region, the average flake size is approximately 4 μm at 180 °C and increases with the sulfur temperature, reaching a peak of 9.8 μm at 250 °C and 11.2 μm at 270 °C. However, beyond 270 °C, the average flake size decreases, dropping to around 4 μm at 300 °C. The MoS_2 flakes in the promoter region are consistently larger than those in the pristine region, with the size difference peaking between 250 °C and 270 °C.

The monolayer ratio, in the pristine region, remains around 5% between 180 °C and 200 °C, reaching a maximum of 20% at 220 °C and 250 °C, and decreasing to 7% at 300 °C. In the promoter region, the monolayer ratio increases steadily with temperature, peaking at 82% at 250 °C, before declining to 48% at 300 °C. The promoter region exhibits a higher monolayer ratio at all temperatures, with the maximum difference between the two regions observed at 250 °C.

The probability of large flakes, on the pristine side, remains steady at around 1.0% between 180 °C and 300 °C. On the promoter side, the probability is 0% at 180 °C, increases to 12.6% at 200 °C, rises significantly to a 35%-50% between 220 to 270 °C, and then decreases to 3.4% at 300 °C. These results show that the promoter region has a higher probability of large flakes, with the maximum occurring between 220 and 270 °C.

The promoter region exhibits significantly higher flake coverage compared to the pristine region within the sulfur temperature range of 200 °C-270 °C, peaking at 250 °C (18%). In contrast, coverage in the pristine region remains relatively low between 0.5%-2% across the temperature range of 180 °C-300 °C. This highlights the enhancement of MoS_2 growth in the promoter region, particularly at a temperature of 250 °C.

The population density, on the pristine side, increases from 0.8×10^3 to 3.1×10^3 mm^{-2} as the temperature rises from 180 °C to 200 °C. However, as the temperature continues to increase, it decreases to 1.3×10^3 mm^{-2} at 220 °C and remains around this value between 220 °C and 300 °C. On the promoter side, except at 180 °C, the population density is lower than that of the pristine side. At 180 °C, the population density on the promoter side is 2.5%, whereas between 200 °C and 300 °C, it ranges from 1.1% to 2.2%.

From the statistical results, the small average size and high population density indicate a high nucleation rate and a low film growth rate in the pristine region. It is evident that MoS_2 2D growth in the promoter region is significantly enhanced, particularly for temperatures between 220 °C and 270 °C, as indicated by increased flake sizes, monolayer ratio, probability of large flakes, and coverage.

To further evaluate the quality of the synthesized MoS_2 under different sulfur temperatures, Raman and PL characterizations are systematically conducted. The average Raman spectra in figure 3(c) obtained from the Raman mappings (figure S12), which are normalized against the Si peak at 520 cm^{-1} and fitted by Lorentzian functions. The normalization removes intensity variations caused by fluctuations in laser power. No detectable Raman peaks are observed at 180 °C, which suggests a limited amount of deposition. The Raman spectra for sulfur temperature between 200 °C to 270 °C exhibit the characteristic E^1_{2g} and A_{1g} modes of MoS_2. For temperatures between 200 °C and 250 °C, the E^1_{2g} is at 383.8 ± 0.7 cm^{-1}, while it redshifts to 381.9 cm^{-1} at 270 °C. The A1g peak is at 406.4 cm^{-1} at 200 °C, which then features a redshift to ~405.2 cm^{-1} at higher sulfur temperatures. The peak difference, $\Delta\omega$, varies accordingly. From 200 °C to 220 °C, the peak difference is around 22.1 cm^{-1}. At 250 °C, the peak difference is 20.8 cm^{-1} which is the minimum among all the samples, indicating the monolayer thickness. When the sulfur temperature exceeds 250 °C, $\Delta\omega$ increases, reaching 24.4 cm^{-1} at 300 °C. The increase in $\Delta\omega$ indicates an increase in MoS_2 thickness [50]. Notably, the E^1_{2g} and A_{1g} peak positions of the sample grown at 250 °C are comparable to those of the ME sample, suggesting that the film quality is close to the ME sample (figure S13).

The average PL spectra in figure 3(d) reveal variations in the Xa exciton energy across different samples. No PL signal is observed from samples grown with a sulfur temperature of 180 °C and 300 °C, indicating poor crystallinity or thick samples. For MoS_2 synthesized at 200 °C, the Xa peak appears at 1.876 eV. As the sulfur temperature increases from 220 °C to 250 °C, the Xa peak redshifts to 1.851 eV and 1.845 eV, respectively. The peak position and intensity of the 250 °C sample is comparable with those of the ME sample, which suggest the sample has minimal impurities and crystallinity. Compared to 250 °C, the blueshift of 0.031 eV observed at 200 °C suggests that oxygen may doped into the film under a sulfur deficient condition, which causes the peak blueshift and enhances the PL intensity [51]. These results indicate that the highest film quality is achieved at 250 °C.

In addition to the main Raman vibration modes of MoS_2 shown in figure 3(c), the LA mode in the frequency region 210-250 cm^{-1} (figure S14) is attributed to the disorder-induced Raman scattering [33], which related with defect structure, such as vacancies, GBs, antisite. The intensity ratio between the LA mode and the E^1_{2g} or A_{1g} mode is inversely proportional to the average inter-defect distance L_D and directly proportional to the defect density, as described by the formula $\frac{I(LA)}{I(X)} = \frac{C(X)}{L_D^2}$ [33]. Figure 3(e) shows the LA/E^1_{2g} peak intensity ratio for the samples prepared at 200 °C–300 °C. The ratio decreases as sulfur temperature increases from 200 °C-250 °C

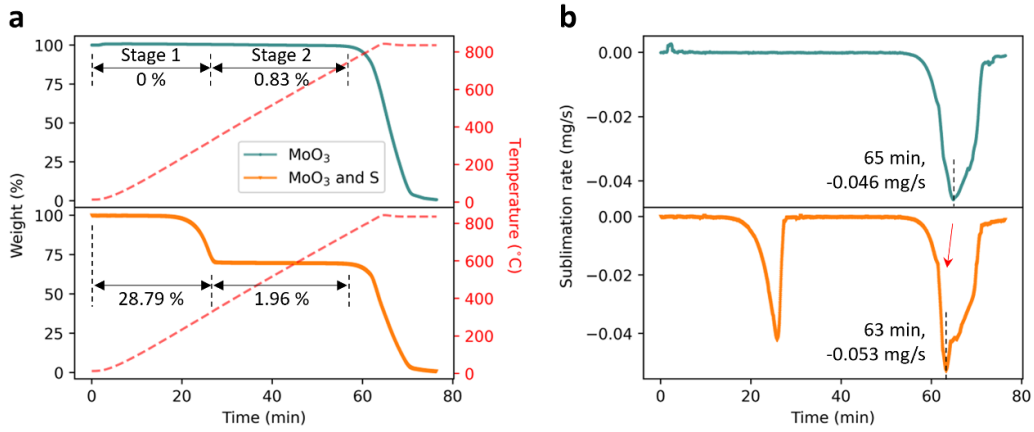

Figure 4. (a) TGA and (b) DTG curves of MoO_3 with and without sulfur.

and rises when the temperature exceeds 250 °C, indicating the lowest defect concentration in the sample at a temperature of 250 °C. On the contrary, the sample prepared at a temperature of 200 °C exhibits the highest LA/E^1_{2g} ratio, reflecting a higher defect density. Since sulfur vacancies are among the most prevalent defects in CVD-grown MoS_2, XPS is employed to characterize the temperature dependence of the sulfur vacancies (figure S15). The integrated intensity of the non-stoichiometric phase MoS_{2-x} is the lowest for the sample at the temperature of 250 °C, which corroborates the Raman defect analysis. The sulfur vacancies in the 200 °C sample are further validated through TEM analysis, as shown in the ACSTEM images (figure S16).

2.3. *Mechanism study*

To explore and understand the significance of promoter and sulfur in the growth process of MoS_2, thermo-gravimetric analysis (TGA) is conducted to compare the thermal behavior of the MoO_3 with and without sulfur, as shown in figure 4(a). The Stage 1, ranging from room temperature to 330 °C, corresponds to sulfur sublimation, while Stage 2 spans from 330 °C to 740 °C, preceding the onset of MoO_3 sublimation. For MoO_3 without sulfur, there is no weight loss during Stage 1 and the weight loss in Stage 2 is 0.83%. In contrast, for the MoO_3 with sulfur, the initial sulfur to total mass ratio is 30.79%. The weight loss of Stage 1 is 28.79% indicating residual sulfur that may form $MoO_{2-x}S_x$. During Stage 2, the weight loss is 1.96%, giving the total weight loss of 30.75% after Stage 2, suggesting that sulfur remains in the compound.

The differential thermo-gravimetric (DTG), or first derivative of the weight with respect to time, curves plotted in figure 4(b) shows that the maximum sublimation rate of MoO_3 is higher in the presence of sulfur (0.053 mg s^{-1}) compared to its absence (0.046 mg s^{-1}). Furthermore, MoO_3 with sulfur reaches its maximum sublimation rate earlier than without sulfur, indicating an acceleration of sublimation. This increased sublimation rate may result from the formation of intermediate product MoO_xS_y [52, 53], which has weaker Mo–S bonds compared to Mo–O bonds [54], facilitating decomposition and sublimation. These findings suggest that the MoO_3 sublimation rate and gas phase concentration can be tuned by the sulfur concentration. In our experiment, the sulfur temperature plays a crucial role in regulating the sulfur evaporation rate. A higher sulfur temperature results in a greater sulfur concentration in the ambient, leading to an increased S-to-Mo ratio. However, TGA/DTA measurements cannot fully capture the complexity of the CVD environment, where factors like gas dynamics, reactor geometry, temperature gradients, and precursor interactions critically influence growth. Nonetheless, TGA/DTA offers valuable qualitative insights into the thermal behavior of MoO_3, aiding the investigation of promoter effects.

The sulfur concentration depends not only on the temperature but also on the presence of nano promoters. The sulfur in the nano promoters (figure S17) locally increases the fractional sulfur concentration, promoting the reduction and sulfurization of MoO_3, thereby facilitating MoS_2 nucleation. In contrast, in the pristine region, the insufficient reduction of MoO_3 results in the formation of MoO_x instead of MoS_2.

Furthermore, decomposition of nano promoters at high temperatures releases carbon, which enhances the reduction of MoO_3 and suppresses the formation of MoO_x. This raises the concern of potential carbon residues contaminating MoS_2. To assess the cleanliness of the polymer-assisted growth, thermal behavior of photoresist S1813 and its role in facilitating MoS_2 growth are examined. The TGA result of S1813 (figure S17(e)) shows a rapid weight loss between 50 °C and 200 °C due solvents and volatile evaporation, followed by a steep decline from 200 °C to 600 °C corresponding to polymer matrix degradation. Beyond 600 °C, gradual weight loss suggests carbonization or decomposition of residual organics, leaving ∼15% mass at 835 °C, attributable to non-volatile inorganic or carbonaceous residue. Raman spectroscopy confirms this residue is carbonaceous (figures S18(b), (f) and (g)). Additional experiments are conducted to compare the behavior of S1813 when heated with S alone or with both S and MoO_3 (see supporting information for details). When only S was added (figures S18 (c), (f) and (g)), the resulting Raman

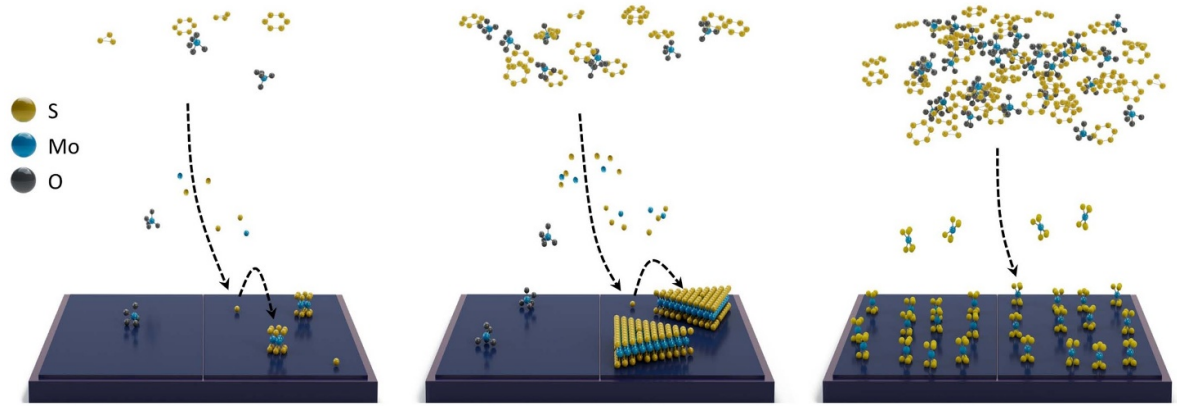

Figure 5. A schematic illustration of the promoter effects at sulfur temperature of 200 °C (left), 250 °C (middle) and 300 °C (right).

spectrum was similar to that without S, indicating that the residue is primarily carbonaceous. In contrast, in the presence of MoO_3 with either insufficient or excessive S (figure S18(d)–(g)), the MoS_2 E^1_{2g} and A_{1g} vibration modes are detected in the Raman spectra, and the peaks between 1200 cm^{-1} and 1800 cm^{-1} disappear indicating the absence of carbon residue. The disappeared carbonaceous can be attributed to a reduction reaction with MoO_3. These results demonstrate that at 835 °C in N_2 atmosphere, S1813 alone or add S only leaves carbonaceous residue, whereas in the presence of S and MoO_3, the carbon act as a reductant, promoting MoO_3 reduction and enabling clean MoS_2 film growth.

Figure 5 presents a schematic illustrating the effects of the promoter at varying sulfur temperatures. At low temperature (e.g. 200 °C), the ambient sulfur concentration is insufficient. In the pristine region, MoS_2 nucleation is hindered due to the sulfur deficiency. In contrast, in the promoter region, sulfur supplied by the nano promoter enables MoS_2 nucleation. However, the overall low sulfur concentration remains inadequate to support extensive film growth. Consequently, the resulting flakes are small and exhibit either a hexagonal geometry or small triangles with rounded edges, which are likely to contain significant sulfur vacancies.

The sulfur concentration increases as the temperature rises to 250 °C. In the promoter region, a consistent and moderate supply of reactants facilitates the 2D film growth with a triangular geometry and fewer defects. Additionally, as previously discussed, the decomposition of the nano promoter at high temperatures provides carbon, which facilitates the reduction of MoO_3 and suppresses the deposition of MoO_x on the substrate. This enhanced reduction of Mo combined with a sufficient supply of reactants, promotes preferential growth in the promoter region.

At higher temperatures (e.g. 300 °C), there is abundant sulfur in the ambient, which also accelerates the consumption of MoO_3, leading to a peak concentration of both S and Mo reactant within a short timeframe. The supersaturated reactant concentration leads to a mass transport-limited CVD process [55], resulting in a high density of particles across the entire substrate, regardless of promoter treatment. This indicates a highly homogeneous nucleation process in both the pristine and promoter regions. Excess reactants spontaneously nucleate numerous MoS_2 particles throughout the substrate, without influence from any foreign surface (e.g. promoters). It is important to note that homogeneous nucleation does not exhibit any preferential attachment to the nano promoters on the substrate, rather it results in a more dispersed distribution of MoS_2 particles. During the nucleation stage, the rapid depletion of S and Mo reactants limits the availability of reactants for further film development.

From our experiments, we found that heterogenous nucleation dominated MoS_2 growth occurs when the sulfur temperature is between 200 °C and 300 °C. This process is regulated by controllable nanoscale promoters in terms of position and density, leading to a more organized and well-structured growth compared to random homogeneous nucleation. We note that surface roughness and energy could also affect nucleation and growth. However, since the majority promoter decomposes before 500 °C, its influence above this temperature is mainly chemical rather than physical.

To evaluate the electrical property of the MoS_2 grown by polymer-assisted method, back-gated field-effect transistor (FET) was fabricated on 285 nm SiO_2/Si substrate using optical lithography. Figure S20 shows the output curve and transfer curve of the device, respectively. The calculated field-effect mobility of 4.1 cm^2 Vs^{-1} and on/off ratio of 10^5 fall within the reported ranges of 0-10 cm^2 Vs^{-1} and 10^5-10^6, respectively [21, 56]. The results indicate that the polymer-assisted method significantly enhances the monolayer MoS_2 growth rate while having a minimal impact on its electrical properties.

3. Conclusion

In summary, we employed nanosized polymer particles as promoters to control the MoS_2 nucleation process, transforming it from homogenous to heterogenous. By controlling the

sulfur temperature, the sulfur partial pressure and the reactant concentration can be tuned. We demonstrate the pivotal role of nanosized polymer promoters in facilitating heterogeneous nucleation while suppressing homogeneous nucleation during the CVD growth of MoS_2. Our findings show that a supersaturated reactant concentration result in excessive homogenous nucleation, regardless of the presence of a polymer promoter, while moderate reactant concentrations facilitate promoter-assisted heterogenous nucleation. The film quality is comprehensively investigated using optical imagery, SEM, PL, AFM, and Raman for the condition of varied reactant concentrations. We found that MoS_2 in the promoter region at a sulfur temperature of 250 °C showed the highest monolayer ratio and minimal defects. This study greatly advances our fundamental understanding of TMD growth mechanisms and opens exciting new avenues for tailored synthesis of TMD materials with enhanced properties, improved material controllability and thus reduced device variability.

4. Methods

4.1. Substrate preparation

S1813 (Shipley) diluted by isopropyl alcohol (IPA, Sigma-Aldrich, 99.8%) with a volume ratio of 1:300 is used as the nano promoter. The Si substrate with a 285 nm SiO_2 layer (1.5×1.5 cm^2) first underwent ultrasonic cleaning, including immersion in acetone for 5 min, followed by a 5 min rinse in IPA, and two subsequent rinses with DI water. After the substrate cleaning process, diluted S1813 was spin-coated (by EMS spinner 4000) on half of the sample with an isolation bar at 5000 revolutions per minute (rpm) for 45 s, followed by baking at 115 °C for 75 s in ambient. The 2 mm wide polydimethylsiloxane (PDMS, Gel-Pak) bar was attached to the middle of the substrate, acting as the boundary between the two regions and preventing the overflow of polymer from one side to the other during the spinning process.

4.2. CVD growth and transfer of MoS_2

The CVD process was conducted in a furnace (MTI GSL-1100X). In a typical growth, N_2 (99.999%) was introduced into the tube inlet as a protective carrier gas. Sulfur powders (MaTecK, 99%, 120 mg) were used as the sulfur source and placed upstream in the tube. MoO_3 powders (Afla Aesar, 99.9%, 1 mg) were dispersed within a 1 cm region in a quartz crucible which is placed at the center of the furnace. The substrate is positioned 0.5 cm downstream from the MoO_3 power and tilted at an angle of 120° relative to the tube axis. The temperature of the MoO_3 and the substrate was controlled by a pre-set heating program. The temperature was first increased from room temperature to 105 °C at a rate of 14 °C min^{-1}, held at 105 °C for 1 h, then further increased to 835 °C, and finally held at 835 °C for 5 min. The sulfur temperature was controlled separately by a heating belt, which was energized when the furnace temperature reached 765 °C. The N_2 flow rate started from 500 sccm, was decreased to 20 sccm when the substrate temperature reached 300 °C and then increased to 500 sccm after the reaction completed.

The MoS_2 was transferred using a polymer assisted method [57]. A polymer resist, polymethyl methacrylate (PMMA, A3), was spun onto the MoS_2 at 3000 rpm for 40 s, followed by a 5 min hot bake. This process forms a polymer film approximately 200 nm in thickness on the sample's surface. Using a razor, approximately 1 mm of the polymer along the chip edge was scratched off to ensure that the polymer film did not adhere to the edge of the chip. Subsequently, the sample was immersed in a saturated sodium hydroxide solution (4M NaOH, Sigma-Aldrich) to etch off the SiO_2 layer. Once the SiO_2 layer was completely dissolved, filter paper was used to retrieve the floating polymer film, which was then rinsed in clean DI water to remove any residual aqueous alkali and neutralize the transferred MoS_2 flakes. After washing, the cleaned film was transferred onto the target substrate. The PMMA film was then removed in acetone for 5 min, washed with IPA for 5 min and DI water for an additional 5 min.

4.3. Characterization

An Olympus BX51M microscope was used to capture the optical images. AFM measurements were conducted on the Oxford Asylum system in tapping mode with Budget Sensors Tap 300 Al-G AFM probe. Raman and PL characterizations were performed using a Witec Alpha 300 R system under a 100× objective lens (NA = 0.95, spot size of ∼0.7 μm) with a 532 nm excitation wavelength laser. The laser power of 3.2 mW was used for the Raman and PL mapping. The SEM images were obtained by using a Zeiss Ultra SEM with a field emission gun under InLens mode with an aperture of 30 μm. The EDX data was collected with a Bruker Nano XFlash 5030 detector integrated with the Zeiss Ultra SEM. XPS measurements were conducted using an Omicron EA 125 Energy Analyzer with a monochromated Al K-alpha source at 1486.7 eV. High-resolution core-level component XPS scans were acquired with a pass energy of 20 eV in high magnification mode, with entrance and exit slits of 6 mm and 3 mm, respectively, giving an overall source and instrument resolution of 0.6 eV. XPS spectra were calibrated to the adventitious carbon C 1 s peak at 285.0 eV. The HRTEM measurements were performed with an uncorrected FEI Titan microscope with a Schottky field emission S-FEG source operated at 300 kV. The AC-STEM were performed on a Nion UltraSTEM 200 microscope equipped with a cold field emission gun and a quadrupole–octupole type probe corrector. The microscope was operated at 60 kV with a 35 mrad convergence semi-angle. TGA measurement was carried out using a Stanton Redcroft STA 1500 (Thorn Scientific, UK) calorimeter with platinum-rhodium crucibles and alumina as a reference. The experiments were carried out with a heating rate of 14 °C min^{-1} in N_2 atmosphere.

4.4. Statistical analysis

OC based analysis and statistical analysis were conducted using Python 3.10. The OC values are cross-checked by AFM (figure S5). The statistical analysis was based on optical images and conducted using Python code. For each temperature, statistical analysis was performed on multiple samples ($n = 4$-6). The average flake size and its standard deviation for each sample were determined by measuring multiple flakes. Considering the image resolution, flakes with a minimum size of 2 μm were included in the statistical count.

4.5. Device fabrication and electrical measurement

Back-gated FET was fabricated on 285 nm SiO_2/Si substrate using optical lithography. A 365 nm light source was used to expose the S1813 photoresist for 6 s through a photomask containing the predefined electrode pattern. The exposed resist was then developed in Microposit MF-319 developer for 45 s. Metallization was performed using an electron beam evaporator (Temescal FC-2000), depositing Ti/Au (1/35 nm) onto the patterned areas. Finally, the lift-off process was carried out by immersing the sample in 1165 remover overnight at room temperature. The electrical data was obtained using Keysight B2912A measurement unit and Yanke probe station YK-ZKTZT in the vacuum.

Data availability statement

All data that support the findings of this study are included within the article (and any supplementary files).

Supplementary Information available at https://doi.org/10.1088/1361-648X/ae14c8/data1.

Acknowledgments

This publication has emanated from research conducted with the financial support of Taighde Éireann-Research Ireland under Grant Number EPSPG/2020/81 and 20/FFP-P/8727. We are pleased to acknowledge the financial support from Intel Ireland. We also extend our thanks to the staffs of the Advanced Microscopy Laboratory (AML) and the Centre for Research on Adaptive Nanostructures and Nanodevices (CRANN) at Trinity College Dublin for their continued technical support.

Conflict of interest

The authors declare no conflict of interest.

Author contributions

L.L.W., Y.S. and K.K. performed the material growth process. L.L.W. and Y.S. carried out the statistical analysis. Raman and PL measurement were conducted by L.L.W., Y.S. and K.K., with assistance from Y.B.Z., while L.L.W. and Y.S analysed the Raman and PL data. AFM measurements were performed by L.L.W. and Y.S., and SEM imaging and EDX measurement were carried out by L.L.W. and H.Z.W. XPS measurement were conducted by L.G. and C.M.G., end TEM measurements were performed by X.Y.G. and V.N. A.R. conducted the TGA measurements. H.Z.Z. and K.G. contributed to the 3D schematic and illustrations. H.Z.Z. developed the Python code with input from L.L.W., Y.S. and K.K. Data analysis was performed collaboratively by L.L.W., Y.S., K.K., N.M., L.G., X.Y.G., and H.Z.Z. The manuscript was written and edited by L.L.W., H.Z.Z., and P.G., with contributions from all authors. H.Z.Z. conceived and supervised the project. All authors discussed the results and provided feedback on the manuscript.

ORCID iDs

Lulin Wang 0000-0001-7814-3245
Kaushik Kannan 0000-0002-4471-836X
Yangbo Zhou 0000-0003-4997-7640
Valeria Nicolosi 0000-0002-7637-4813
Hongzhou Zhang 0000-0002-1188-7810

References

[1] Li M-Y, Su S-K, Wong H-S P and Li L-J 2019 *Nature* **567** 169
[2] Liu Y, Duan X, Shin H-J, Park S, Huang Y and Duan X 2021 *Nature* **591** 43
[3] Mak K F, Lee C, Hone J, Shan J and Heinz T F 2010 *Phys. Rev. Lett.* **105** 136805
[4] Radisavljevic B, Radenovic A, Brivio J, Giacometti V and Kis A 2011 *Nat. Nanotechnol.* **6** 147
[5] Jadwiszczak J *et al* 2018 *Sci. Adv.* **4** eaao5031
[6] Jayachandran D, Oberoi A, Sebastian A, Choudhury T H, Shankar B, Redwing J M and Das S 2020 *Nat. Electron.* **3** 646
[7] Jadwiszczak J, Li G, Cullen C P, Wang J J, Maguire P, Duesberg G S, Lunney J G and Zhang H 2019 *Appl. Phys. Lett.* **114** 091103
[8] Barth I *et al* 2024 *ACS Nano* **18** 12897
[9] Jadwiszczak J *et al* 2019 *ACS Nano* **13** 14262
[10] Jiang J, Guo J, Wan X, Yang Y, Xie H, Niu D, Yang J, He J, Gao Y and Wan Q 2017 *Small* **13** 1700933
[11] Mohapatra P K, Ranganathan K and Ismach A 2020 *Adv. Mater. Interfaces* **7** 2001549
[12] Xia Y *et al* 2023 *Nat. Mater.* **22** 1324
[13] Yu H *et al* 2017 *ACS Nano* **11** 12001
[14] Li T *et al* 2021 *Nat. Nanotechnol.* **16** 1201
[15] Yu H *et al* 2024 *Adv. Mater.* **36** e2402855
[16] Jiang H *et al* 2025 *Nat. Mater.* **24** 188–96
[17] Singh A, Sharma M and Singh R 2021 *Cryst. Growth Des.* **21** 4940
[18] Kim H, Ovchinnikov D, Deiana D, Unuchek D and Kis A 2017 *Nano Lett.* **17** 5056
[19] Kim H *et al* 2017 *Nanotechnology* **28** 36LT01
[20] Li S, Wang S, Xu T, Zhang H, Tang Y, Liu S, Jiang T, Zhou S and Cheng H 2021 *Nanoscale* **13** 13030
[21] Zhang K *et al* 2018 *ACS Appl. Mater. Interfaces* **10** 40831
[22] Lee Y-H *et al* 2012 *Adv. Mater.* **24** 2320
[23] Lee Y-H *et al* 2013 *Nano Lett.* **13** 1852

[24] Ling X, Lee Y-H, Lin Y, Fang W, Yu L, Dresselhaus M S and Kong J 2014 *Nano Lett.* **14** 464
[25] Yang H, Giri A, Moon S, Shin S, Myoung J-M and Jeong U 2017 *Chem. Mater.* **29** 5772
[26] Campbell S A 2001 *The Science and Engineering of Microelectronic Fabrication* (*Oxford series in electrical and computer engineering*) (Oxford University Press)
[27] Zhang H Z, Wang L L, Sun Y and Kannan K 2024 Python code for statistical analysis (available at: https://github.com/Lulin-66/MS-Data-analysis)
[28] Li H, Zhang Q, Yap C C R, Tay B K, Edwin T H T, Olivier A and Baillargeat D 2012 *Adv. Funct. Mater.* **22** 1385
[29] Yu Y, Li C, Liu Y, Su L, Zhang Y and Cao L 2013 *Sci. Rep.* **3** 1866
[30] Jeon J, Jang S K, Jeon S M, Yoo G, Jang Y H, Park J-H and Lee S 2015 *Nanoscale* **7** 1688
[31] Carvalho B R, Malard L M, Alves J M, Fantini C and Pimenta M A 2015 *Phys. Rev. Lett.* **114** 136403
[32] Schaefer C M, Caicedo Roque J M, Sauthier G, Bousquet J, Hébert C, Sperling J R, Pérez-Tomás A, Santiso J, Del Corro E and Garrido J A 2021 *Chem. Mater.* **33** 4474
[33] Mignuzzi S, Pollard A J, Bonini N, Brennan B, Gilmore I S, Pimenta M A, Richards D and Roy D 2015 *Phys. Rev. B* **91** 195411
[34] Fu W, John M, Maddumapatabandi T D, Bussolotti F, Yau Y S, Lin M and Johnson Goh K E 2023 *ACS Nano* **17** 16348
[35] Karvonen L *et al* 2017 *Nat. Commun.* **8** 15714
[36] Kaasbjerg K, Thygesen K S and Jacobsen K W 2012 *Phys. Rev. B* **85** 115317
[37] Backes C *et al* 2014 *Nat. Commun.* **5** 4576
[38] Zhu Y *et al* 2023 *ACS Nano* **17** 13545
[39] Jadkar V, Pawbake A, Waykar R, Jadhavar A, Mayabadi A, Date A, Late D, Pathan H, Gosavi S and Jadkar S 2017 *J. Mater. Sci., Mater. Electron.* **28** 15790
[40] Kumar Singh Patel S, Dewangan K, Kumar Srivastav S, Verma N K, Jena P, Kumar Singh A and Gajbhiye N S 2018 *Adv. Mater. Lett.* **9** 585
[41] Feng N, Meng R, Zu L, Feng Y, Peng C, Huang J, Liu G, Chen B and Yang J 2019 *Nat. Commun.* **10** 1372
[42] Grey L H, Nie H-Y and Biesinger M C 2024 *Appl. Surf. Sci.* **653** 159319
[43] Liang T *et al* 2020 *ACS Appl. Electron. Mater.* **2** 1055
[44] Geng D Z *et al* 2016 *2D Mater.* **4** 011012
[45] Zhi Q, Jiang R, Yang X, Jin Y, Qi D, Wang K, Liu Y and Jiang J 2024 *Nat. Commun.* **15** 678
[46] Gaur A P S, Sahoo S, Ahmadi M, Dash S P, Guinel M J-F and Katiyar R S 2014 *Nano Lett.* **14** 4314
[47] Li Y, Hao S, DiStefano J G, Murthy A A, Hanson E D, Xu Y, Wolverton C, Chen X and Dravid V P 2018 *ACS Nano* **12** 8970
[48] Govind Rajan A, Warner J H, Blankschtein D and Strano M S 2016 *ACS Nano* **10** 4330
[49] Cao D, Shen T, Liang P, Chen X and Shu H 2015 *J. Phys. Chem. C* **119** 4294
[50] Lee C, Yan H, Brus L E, Heinz T F, Hone J and Ryu S 2010 *ACS Nano* **4** 2695
[51] Nan H A W *et al* 2014 *ACS Nano* **8** 5738
[52] Hong S *et al* 2018 *J. Phys. Chem. C* **122** 7494
[53] Hong S, Krishnamoorthy A, Rajak P, Tiwari S, Misawa M, Shimojo F, Kalia R K, Nakano A and Vashishta P 2017 *Nano Lett.* **17** 4866
[54] Western S S 2009 X-ray photoelectron spectroscopy (XPS) reference pages (available at: www.xpsfitting.com/2009/10/molybdenum.html)
[55] Ohring M 2001 *Materials Science of Thin Films: Depositon and Structure* (Elsevier) (https://doi.org/10.1016/B978-0-12-524975-1.X5000-9)
[56] Zhan Y, Liu Z, Najmaei S, Ajayan P M and Lou J 2012 *Small* **8** 966
[57] Bie Y-Q *et al* 2011 *Adv. Mater.* **23** 3938